

# MHD Modeling for Formation Process of Coronal Mass Ejections: Interaction between Ejecting Flux Rope and Ambient Field

Daikou Shiota<sup>1</sup>, Kanya Kusano<sup>2,3</sup>, Takahiro Miyoshi<sup>4</sup>, Kazunari Shibata<sup>5</sup>,

## ABSTRACT

We performed magnetohydrodynamic simulation of a formation process of coronal mass ejections (CMEs), focusing on interaction (reconnection) between an ejecting flux rope and its ambient field. We examined three cases with different ambient fields: no ambient field, and cases with dipole field of two opposite directions which are parallel and anti-parallel to that of the flux rope surface. As a result, while the flux rope disappears in the anti-parallel case, in other cases the flux ropes can evolve to CMEs and show different amounts of rotation of the flux rope. The results imply that the interaction between an ejecting flux rope and its ambient field is an important process for determining CME formation and CME orientation, and also show that the amount and direction of magnetic flux within the flux rope and the ambient field are key parameters for CME formation. Especially, the interaction (reconnection) plays a significant role to the rotation of the flux rope, with a process similar to “tilting instability” in a spheromak-type experiment of laboratory plasma.

*Subject headings:* magnetic reconnection — magnetohydrodynamics (MHD) — Sun: corona — Sun: coronal mass ejections (CMEs)

---

<sup>1</sup>Advanced Science Institute, RIKEN (Institute of Physics and Chemical Research), Wako, Saitama 351-0198 Japan; shiota@riken.jp

<sup>2</sup>Solar-Terrestrial Environment Laboratory, Nagoya University, Furo-cho, Chikusa-ku, Nagoya, 464-8601, Japan

<sup>3</sup>Japan Agency for Marine-Earth Science and Technology (JAMSTEC), Kanazawa, Yokohama, Kanagawa 236-0001, Japan

<sup>4</sup>Graduate School of Science, Hiroshima University, Kagamiyama, Higashi-Hiroshima, Hiroshima, 739-8526, Japan

<sup>5</sup>Kwasan and Hida Observatories, Kyoto University, Yamashina, Kyoto, 607-8471, Japan

## 1. Introduction

Coronal mass ejections (CMEs) are one of the most spectacular explosive phenomena in which large amounts of mass and magnetic flux are ejected to the interplanetary space. CMEs are believed to be consequences of sudden release of magnetic energy, i.e., disruptions of coronal magnetic field, as same as flares which are strong brightening observed in soft x-ray. The energy released upward can be converted to kinetic energy as ejected flux ropes and/or CMEs, while energy released downward can be converted to thermal energy or high energy particles. Therefore larger flares show higher association rate with CMEs (Kahler 1992; Kim et al. 2005; Yashiro et al. 2005), but they do not necessarily accompany each other. Association of flares can be explained by energy release rate which depends on the condition of coronal plasma. If the energy release is fast enough to heat chromospheric plasma, the heated plasma fills above coronal loops, which are accompanied with strong brightening in soft x-ray observed as flares. If the energy release is not fast enough to overcome radiative energy loss, the strong brightening does not occur. In the same time, if ejecting structures successfully escape to interplanetary, the event can be understood as CMEs without flares. On the other hand, in some cases, if an ejection associated with a strong soft x-ray brightening, cannot escape to the interplanetary space, the event should be observed as a flare without CME (Yashiro et al. 2006).

The disruptions of coronal magnetic field are observed to occur commonly in a wide spatial range. *Yohkoh* satellite reveals that faint giant coronal arcades which are similar to flares are formed associated with CMEs (Hiei et al. 1993; McAllister et al. 1996). On the other hand, the similar evolutions where flares occurs with mass (plasmoid) ejections are observed accompanied much smaller scale emerging flux (Sakajiri et al. 2004). Based on such observational evidence, Shibata (1999) proposed that giant arcades, flares, mass ejections, and CMEs are understood with an unified view so-called 'flares'. The model is supported by the statical characteristic of flares. Solar flares show a “power-law” distribution between their energy scales and occurrence rate (Drake 1971; Datlowe et al. 1974; Dennis 1985; Shimizu 1995).

In contrast to flares, CMEs show log-normal distribution between the energy scales and the event number (Aoki et al. 2004; Yurchyshyn et al. 2005; Lara et al. 2006). Statistical characteristics of CMEs and flares are different in spite of their common origin. This difference in statistical distribution means the existence of some kinds of filter effects which prevent small scale mass ejections to evolve CMEs selectively. Candidates of such filter effects are interactions between eruptions and their ambient magnetic field whose spatial scale is larger than that of the eruption regions. Important points in formation process of CMEs can be not only the formation of ejecting structures (flux rope) but also whether they

overcome the obstacles.

Trigger processes of such eruptions have been numerically investigated for a few decades (Forbes & Priest 1995; Antiochos et al. 1999; Chen & Shibata 2000; Kusano et al. 2004; Kliem & Török 2006). In “breakout” model (Antiochos et al. 1999), the interaction between a sheared arcade and its ambient field is considered to play a fundamental role for the triggering. In the model, the field configuration is assumed to be favorable to reconnection between the erupting sheared arcade and its ambient field. During the eruption the reconnection can reduce the poloidal magnetic flux of the flux rope which is supplied by another reconnection occurred inside the sheared arcade. As the results of competition between the magnetic flux reduction and the supply, an eruption is capable of failing to produce a CME. In some other models (Forbes & Priest 1995; Kusano et al. 2004; Inoue & Kusano 2006; Kliem & Török 2006) ideal MHD processes (loss of equilibrium or instability) of detached flux ropes are dominant in the trigger processes. In such models, the direction of its ambient field can be independent of the trigger processes. If the direction of the ambient field is favorable to reconnection, the reconnection can reduce the magnetic flux as mentioned above. In contrast, if the direction is parallel to the poloidal flux the ambient field can drag and stop the ejecting flux rope (Choe & Lee 1996; Shiota et al. 2008). Hence the interactions between ejecting flux ropes and their ambient field can be a key factor for formation of CMEs.

From the point of view of space weather science, when CMEs containing southward magnetic flux impact the Earth magnetosphere, they make large influences on the space environment near the Earth. Hence, it is also important for space weather forecast to understand the whole evolution process of CMEs; how CMEs are formed and how much southward magnetic flux CMEs contain when they reach to the orbit of the Earth. Estimation of southward magnetic flux is a complicated task important for space weather, and requires understanding of initial conditions and whole evolution processes of eruptions. For example, in nonlinear evolution of kink instability of a strongly twisted flux rope, its untwisting (writhe) motion can rotate the flux rope (Kliem et al. 2004; Török & Kliem 2005). The ejecting twisted flux ropes could change their directions due to the writhe rotations since their onset or formation if the ropes become unstable in the mode.

Rotations of ejecting flux ropes are reported in CME observations. Yurchyshyn (2008) investigated the angles of magnetic clouds, halo CME axes derived from coronagraph images, and EUV post-eruptive arcade axes in CME source regions. They found that there are good correlation of angles between the axis of EUV arcades and CMEs, and that between axes of magnetic clouds and coronal neutral lines (Heliospheric current sheets), while there is low correlation of angles between CMEs and magnetic clouds. The fact means that some fraction of ejected magnetic structures are significantly rotated during the travel from the

solar corona to 1 AU. During the way, the ambient field should be of two type of structure; closed and open. In the outer corona or interplanetary, all magnetic field should be open due to dragging of the solar wind while most of magnetic field lower corona should be closed. The rotation may result from the interactions with the both type of ambient field. Especially, Yurchyshyn (2008) reported that a few events show the deviation between the neutral line angles of post eruptive arcades (in lower corona) and the axes of CMEs (in a few solar radii). This means that the rotation during the evolution in lower corona, i.e., interaction with closed field, is not negligible.

In this study, we performed a three-dimensional MHD simulation of a twisted flux rope ejected from an active region surrounded by a global ambient magnetic field. According to the numerical results, we discuss the condition for formation of CMEs and evolutions of CME magnetic field structures, focusing on the interactions between ejecting flux ropes and their ambient closed field.

In the next section, we describe the detailed methodology of the numerical simulation. In section 3, the numerical results of different ambient field are shown. We discuss the quantitative relations suggested by the numerical results in §4. Finally, we summarize this paper in §5.

## 2. Numerical Model

### 2.1. Numerical Scheme

We performed three dimensional MHD simulation which solves time variation of 8 physical quantities; density, gas pressure, velocity and magnetic field ( $\rho$ ,  $p$ ,  $\mathbf{v}$ , and  $\mathbf{B}$ , respectively). In order to simplify the MHD equations, the 8 physical quantities are normalized with the following typical values in the corona:  $L_0 = R_\odot = 6.99 \times 10^5$  [km],  $B_0 = 30$  [Gauss],  $\rho_0 = m_H \times 10^9 = 1.67 \times 10^{-15}$  [g cm<sup>-3</sup>],  $v_0 = V_{0,A} = B_0/\sqrt{4\pi\rho_0} = 2071$  [km s<sup>-1</sup>], as these results,  $\tau_0 = \tau_A = 350$  [s],  $p_0 = \rho_0 V_{0,A}^2 = 7.16 \times 10^1$  [erg cm<sup>-3</sup>]. The normalized MHD equations (equation of continuity, equation of motion, induction equation, and equation of energy with gravity) are expressed as follows:

$$\frac{\partial \rho}{\partial t} + \nabla \cdot (\rho \mathbf{v}) = 0, \quad (1)$$

$$\frac{\partial \rho \mathbf{v}}{\partial t} + \nabla \cdot (\rho \mathbf{v} \mathbf{v} - \mathbf{B} \mathbf{B} + p_T \mathbf{I}) = \rho \mathbf{g}, \quad (2)$$

$$\frac{\partial \mathbf{B}}{\partial t} + \nabla \cdot (\mathbf{B} \mathbf{v} - \mathbf{v} \mathbf{B} + \psi \mathbf{I}) = -\nabla \times (\eta \mathbf{J}), \quad (3)$$

$$\frac{\partial e}{\partial t} + \nabla \cdot [(e + p_T)\mathbf{v} - (\mathbf{v} \cdot \mathbf{B})\mathbf{B}] = 0, \quad (4)$$

where

$$\mathbf{J} = \nabla \times \mathbf{B}, \quad (5)$$

$$e = \frac{\rho \mathbf{v}^2}{2} + \frac{p}{\gamma - 1} + \frac{\mathbf{B}^2}{2} + \frac{G_0}{r} \rho, \quad (6)$$

$$p_T = p + \frac{\mathbf{B}^2}{2}, \quad (7)$$

$$\mathbf{g} = -G_0 \mathbf{r} / r^3, \quad (8)$$

$$G_0 = \frac{GM_\odot}{R_\odot v_0^2}, \quad (9)$$

$G$  is gravitational constant,  $\mathbf{I}$  is the unit matrix in the Cartesian coordinate,  $\psi$  is additional variables described below, and  $M_\odot$  is mass of the Sun. Divergence operator is solved by a finite volume method with the HLLD nonlinear Riemann solver (Miyoshi & Kusano 2005) which is combined with the 3rd order Monotone Upstream-centered Schemes for Conservation Laws (MUSCL) developed by van Leer (1979) and the 2nd order Runge-Kutta time integration. Specific heat ratio  $\gamma$  is set to be 1.05 which means an additional heat source. Resistivity  $\eta$  is set to be 0 which means reconnection is caused by the numerical diffusion.

Generally, the results of time integration of equation (3) multi-dimensional MHD simulation is possible to cause numerical  $\nabla \cdot \mathbf{B}$  due to discretization of numerical domain. The equations (2), (3), and (4) are derived with Solenoidal condition, and therefore such finite numerical  $\nabla \cdot \mathbf{B}$  can break down the simulation. In order to keep the numerical  $\nabla \cdot \mathbf{B}$  to be sufficiently small value, we applied an additional variable  $\psi$  and additional equation,

$$\frac{\partial \psi}{\partial t} + c_h^2 \nabla \cdot \mathbf{B} + c_h^2 / c_p^2 \psi = 0 \quad (10)$$

based on the hyperbolic divergence B cleaning method (Dedner et al. 2002). The coefficient  $c_h$  in Equation (10) is propagation speed of the numerical  $\nabla \cdot \mathbf{B}$ , and the coefficient  $c_p$  is diffusion coefficient of  $\psi$ . This numerical methods are described more in Shiota et al. (2008).

The numerical domain is a spherical shell of  $(r_{\min}, r_{\max}) = (1.01, 5.0)$ . The domain is discretized with Yin-Yang grid (Kageyama & Sato 2004), a chimera grid composed of two congruence spherical partial shells ( $\pi/4 \leq \theta \leq 3\pi/4, -3\pi/4 \leq \phi \leq 3\pi/4$ ) each of which is installed in different direction. The physical quantities on the edges of the each partial shell are substituted by interpolated values at the same position in the counterpart shell.

Thus the boundary condition in this grid system only at inner and outer edges for the radial direction. The inner boundary is assumed to be the line-tying wall, where  $B_{\text{norm}}$  is

constant and  $\mathbf{v} = 0$ . The outer boundary is assumed to be the free boundary, where the radial gradients of all quantities are zero.

Note that, in this simulation, test particles which are distributed in some manners in initial condition are advected with plasma bulk flows. The magnetic field lines in Figures in this paper are obtained with the integration of the magnetic field from the position of the test particles of each time step. Thus we capture the evolution of individual magnetic field lines with this technique.

## 2.2. Initial condition

The subject of the present work is to understand how a flux rope ejected from an active region evolves to a CME. The initial magnetic field consists of the ejecting flux rope ( $\mathbf{B}_S$ ) and ambient global field ( $\mathbf{B}_D$ ). We performed three cases of simulation where only the ambient field  $\mathbf{B}_D$  is different. The ambient global field ( $\mathbf{B}_D$ ) is chosen to be simple dipole field:

$$B_{r,D}(r, \theta, \phi) = \frac{2B_D \sin \theta}{3r^3} \quad (11)$$

$$B_{\theta,D}(r, \theta, \phi) = \frac{B_D \cos \theta}{3r^3}. \quad (12)$$

In order to study the interaction between an ejected flux rope and ambient field, we carried out three cases of simulation with different strength and direction of the ambient fields, i.e., their amplitude  $B_D$  of  $0.0, -B_{D,0}$ , and  $B_{D,0}$ , which are labeled with case A, B, and C, respectively.  $B_{D,0} = 0.124$  (3.72 [G]) is a base field strength of the corona where the Alfvén speed is equal to the sound speed of  $T = 2 \times 10^6$  [K].

We mimic the ejected flux rope formed as a result of eruption in an active region with a spheromak type magnetic field which is a linear force-free field in a completely isolated sphere (see Figure 1a).

$$\mathbf{B}_S(r, \theta, \phi) = \tilde{\mathbf{B}}(\tilde{r}, \tilde{\theta}, \tilde{\phi}), \quad (13)$$

where  $\tilde{\mathbf{r}} = \alpha(\mathbf{r} - \mathbf{r}_S)$  is the translated and rescaled local spherical coordinate whose origin corresponds to the center of the spheromak. The spheromak type field is expressed as follows:

$$\tilde{B}_{\tilde{r}}(\tilde{r}, \tilde{\theta}, \tilde{\phi}) = -2B_{S0} \frac{j_1(\tilde{r})}{\tilde{r}} \cos \tilde{\theta}, \quad (14)$$

$$\tilde{B}_{\tilde{\theta}}(\tilde{r}, \tilde{\theta}, \tilde{\phi}) = B_{S0} \left( \frac{j_1(\tilde{r})}{\tilde{r}} + j_1'(\tilde{r}) \right) \sin \tilde{\theta}, \quad (15)$$

$$\tilde{B}_{\tilde{\phi}}(\tilde{r}, \tilde{\theta}, \tilde{\phi}) = B_{S0} j_1(\tilde{r}) \sin \tilde{\theta}, \quad (16)$$

where  $B_{S0}$  is field strength of the spheromak and  $j_1$  and  $j_1'$  are first order spherical Bessel function and its derivative:

$$j_1(x) = \frac{\sin x - x \cos x}{x^2}, \quad (17)$$

$$j_1'(x) = \frac{2x \cos x - (x^2 - 2) \sin x}{x^3}. \quad (18)$$

We adopt only the field within the isolated spherical shell  $\tilde{r} \leq \tilde{a}$  (transparent sphere in Figure 1a) while  $\tilde{\mathbf{B}}_S = 0$  outside of the shell. As definition of the spherical Bessel function,  $\tilde{a} = 4.493409458$  and  $\alpha = \tilde{a}/a_S$ . The toroidal flux ( $\Phi_S$ ) and poloidal flux ( $\Phi_P$ ) of this field are obtained by numerical integrations;

$$\Phi_S = \int_0^\pi d\tilde{\theta} \int_0^{a_S} \tilde{r} \tilde{B}_{\tilde{\phi}} d\tilde{r} = 0.261 a_S^2 B_{S0}, \quad (19)$$

$$\Phi_P = \int_{-\pi}^\pi d\tilde{\phi} \int_0^{a_S} \frac{\tilde{r}}{2} \left| \tilde{B}_\theta \left( \tilde{\theta} = \frac{\pi}{2} \right) \right| d\tilde{r} = 0.0736 a_S^2 B_{S0}. \quad (20)$$

In the present paper, we choose the position of the center of the spheromak  $\mathbf{r}_S = (1.1, \pi/2, 0)$  in the spherical coordinate (on the  $x$  axis), and the major axis of turns is parallel to the  $z$  axis. The radius of the spheromak  $a_S = 0.2$ , i.e.,  $1.4 \times 10^{10}$  [cm]. Here, we assume the toroidal flux of the spheromak  $\Phi_S = 0.0174 = 2.55 \times 10^{21}$  [mx] which is a typical amount of magnetic flux within a CME (Kataoka et al. 2009). Then Equation (19) yields the field strength of the spheromak  $B_{S0} = \Phi_S / (0.261 a_S^2) = 1.67 = 50$  [Gauss].

Although a spheromak is a linear force-free field, we adopt it only within the boundary  $\tilde{r} \leq \tilde{a}$ . At the spherical boundary  $\tilde{r} = \tilde{a}$ , the local radial ( $\tilde{B}_{\tilde{r}}$ ) and azimuthal ( $\tilde{B}_{\tilde{\phi}}$ ) components vanish and then only the local zenithal component  $\tilde{B}_{\tilde{\theta}}$  exists while  $\tilde{\mathbf{B}} = 0$  outside of the boundary. Therefore the force does not balance at the spherical boundary, i.e., a strong outward gradient of magnetic pressure exists there. The Lorentz force due to the current which corresponds to a steep magnetic pressure gradient causes the strong expansion. The spheromak field naturally swells in the simulation.

Figures 1 shows schematic pictures of magnetic field direction on the meridional plane through the center of in cases B (1b) and C (1c). The spheromak local zenithal field on its surface  $\tilde{r} = \tilde{a}$  satisfies  $\tilde{B}_{\tilde{\theta}}(\tilde{r} = \tilde{a}) \geq 0$  (cf. eq. (15)), which is southward. On the other hand, the ambient field is northward ( $B_D < 0$ ) in case B, while it is southward in cases C. On the equator,  $\tilde{B}_{\tilde{\theta}}(\tilde{r} = \tilde{a})$  and  $B_{\theta,D} < 0$  becomes anti-parallel in case B, while parallel in case C. Hence, cases A, B, and C are referred as ‘no ambient’ ‘anti-parallel’, and ‘parallel’ cases in this paper.

Density and pressure are determined by hydrostatic equilibrium with uniform temper-

ature  $T = 2 \times 10^6$  [K],

$$p = p_b \exp \left[ \frac{G_0 \gamma}{p_b} \left( \frac{1}{r} - 1 \right) \right] \quad (21)$$

$$\rho = \gamma \frac{p}{p_b} \quad (22)$$

$$\mathbf{v} = 0, \quad (23)$$

where  $p_b = 2\rho_0 k_B T / (m_H p_0)$  is the normalized pressure on solar surface ( $r = 1$ ). In the present study, we did not apply the solar wind, which is also important factor for the formation of a CME. This is because we intend to purely investigate the interaction between the ejecting and the ambient fields in the early phase of the CME formation.

### 3. Numerical Results

#### 3.1. Common evolution

In all cases, the spheromak (flux rope) initially swells outward due to the non-equilibrium initial condition and the line-tying boundary as described in the previous section. At the same time, the expanding flux rope also shows the similar rotation around the line of the ejection in all case. This rotation is caused by an untwisting (writhe) motion of the highly twisted initial spheromak structure (see Figure 1a).

In order to show the height-time evolution, the right panels of Figure 2 illustrate time variation of plasma  $\beta \equiv 0.5p/B^2$  along the  $x$  axis. The low plasma  $\beta$  regions along the  $x$  axis express the positions of the flux rope. Therefore the low plasma  $\beta$  in the height-time diagrams illustrated in Figure 2 corresponds to the trajectories of the flux ropes. In all the cases the flux rope rapidly expands just after the start, followed by rising and expanding motion with some deceleration.

In all the cases, many small features appear around the altitude  $r \sim 1.1$  and rise as time below the flux rope in the right panels of Figure 2. These structures are small plasmoids formed by tearing of the current sheet between the anchored axial flux. Once such plasmoids are formed in the current sheet, due to gradient of magnetic pressure, they are ejected to upper direction, and finally collide and coalesce into the above flux rope. However, the momentum and energy additions by the plasmoids are too small to accelerate the flux rope. The evolution is similar to the results of 2D simulation (Shiota et al. 2008).

### 3.2. ‘No ambient’ case

In ‘no ambient’ case (case A), the flux rope can expand into unmagnetized plasma. We simulated this case as a reference case with no magnetic obstacle. The expanding flux rope drags outward its anchored axial flux. The dragged axial flux forms  $\Omega$ -shape and at the center of them a current sheet is formed. Although the reconnection occurs between the dragged fluxes, a part of the flux remains anchored.

Figures 2a and 2b show the magnetic field structure at  $t = 50$  (well-developed phase) and the height-time diagrams in this case. Figure 2b expresses the time evolution of the flux rope in this case. The flux rope rapidly expands just after the start ( $t \lesssim 10$ : early phase), and then it shows rising and expanding motion during middle phase ( $10 \lesssim t \lesssim 30$ ). The flux rope is slightly decelerated. In the late phase ( $t \gtrsim 30$ ), the flux rope expands self-similarly at almost a constant speed, and finally reaches the outer boundary of the numerical domain.

### 3.3. ‘Anti-parallel’ case

We simulated the ‘anti-parallel’ case (case B) as a condition where the directions of poloidal fluxes of the ejection and the ambient field are opposite. Such a condition is probable if the flux rope is formed and ejected in a newly emerged flux system whose direction is opposite to the pre-existing ambient field. This situation is modeled as a candidate system for rapid eruption for a CME (Antiochos et al. 1999).

The time evolution of the flux rope is significantly different from that in case A. Because the direction of the ambient field is opposite to the poloidal field of the ejecting flux rope, there is a strong current sheet where magnetic reconnection occurs. Similar to the scenario of Antiochos et al. (1999), the rise motion of the flux rope presses the current sheet, and then enhances its current density, i.e., the reconnection rate there. However, the poloidal flux of the flux rope is peeling off due to the reconnection with the ambient as it rises. Finally, as shown in Figure 2c, after most of the poloidal flux is reconnected, the flux rope no longer exists. The magnetic flux becomes just coronal loops within which shear Alfvén waves propagate. Such a result may be a candidate condition for plasmoid ejections (flares) without CMEs.

We can see the time evolution of the flux rope in height-time diagram (Figure 2d). In the early phase ( $t \lesssim 10$ ), the trajectory and the vertical size are similar to those in case A. After the phase, the top edge of the flux rope becomes lower than that in case A because of the flux peeling ( $10 \lesssim t \lesssim 35$ : middle phase). Finally ( $t \gtrsim 35$ : late phase), the plasma  $\beta$  inside the flux rope becomes comparable to unity, it stays almost the same height. In this

phase, the structure is recognized as twisted loops rather than a flux rope.

### 3.4. ‘Parallel’ case

We simulated the ‘parallel’ case (case C) as a condition where the directions of poloidal fluxes of the ejection and the ambient field are parallel. CME formation process in a similar but axisymmetric situation is studied by Shiota et al. (2008). The present study is an extension of Shiota et al. (2008) to study three-dimensionality of CME formation process.

The time evolution of the flux rope is a little different from that in case A, as shown in Figure 2e and 2f. In the early phase ( $t \lesssim 10$ ), the flux rope rapidly expands, and shows rising and expanding motion during in the middle phase ( $10 \lesssim t \lesssim 45$ ), and then a self-similar evolution in the late phase ( $t \gtrsim 35$ ). The expanding flux rope forms an  $\Omega$ -shape loop and its central current sheet where magnetic reconnection occurs, and finally the flux rope reaches the outer boundary, similar to in case A. In contrast to the result of case A, the ejecting flux rope is significantly deformed (Figures 2a and 2e), although the flux rope is successfully ejected to the outer boundary in both cases. The difference should be caused by reconnection between the flux rope and the ambient magnetic field. The height evolution of the flux rope is similar to that in case A but the flux rope continues to be decelerated (Figures 2b and 2f).

We investigated the time evolution of the magnetic field configuration. Figure 3 and 4 shows the time evolution of the magnetic field configuration seen from the side and the face of the ejecting flux rope. Some characteristic field lines are highlighted with colors (green, light blue, blue, and red) in the figures. These lines are drawn by integrating magnetic field from the same points on the inner boundary in each time step.

The “green” field line represents the initial axial field line. As the flux rope expands, the axial field lines are dragged and stretched as shown in Figure 3a - 3e. Finally the field line reconnects at the  $\Omega$ -shaped center as described in §3.2.

The “light blue” field line indicates “interchanged field line”. The line is initially an ambient field line (Figure 3a and 4a). As the flux rope expands, the line is pushed aside by the flux rope (Figure 3b and 4b). Because the direction of magnetic field is parallel, the ambient field line does not reconnect with the flux rope. However, as the flux rope evolves, it rotates due to writhe motion. The field lines are connected to inside of the flux rope (Figure 3c and 4c). The result implies that the field lines reconnect with the flux rope at the current sheets formed on the flux rope surface. The location of the reconnection is examined later (§4.2).

The “blue” field line indicates also “interchanged field line”. The line is also initially an ambient field line further than “light blue” line. The “blue” field line reconnects with the ejecting flux rope at the current sheet formed on its surface as same as the “light blue” field line.

Reconnection occurs also in the front of the flux rope. In the initial condition, the poloidal field of the surface of the flux rope is parallel to the ambient field. As mentioned in §3.1, however, the flux rope rotates due to its writhe motion. The direction of magnetic field on the flux rope front rotates counterclockwise as shown in Figure 4. The rotation cause the formation of a current sheet on the front and then magnetic reconnection occurs there.

See the “red” field line in Figure 3 and 4. The “red” line was initially ambient dipole field but finally connected to the inside of the flux rope, i.e., becomes the new axial field of the ejecting flux rope (Figure 3f and 4f).

## 4. Discussion

### 4.1. Magnetic Flux relation for CME formation

The amounts of magnetic flux and magnetic helicity are key parameters to understand the numerical results. Here we estimate the amounts of magnetic flux and helicity and discuss the relation between them and a condition for CME formation. In the initial conditions of case B and C, though the spheromak field structure is superposed into the ambient dipole field, the ambient dipole field component is so weak that it does not change the spheromak field. Hence we can regard the time evolutions in case B and C as the results from the interaction (reconnection) between ejecting flux rope and the ambient field.

Whether an ejecting flux rope can evolve to a CME depends on the magnetic flux relation of the overlying ambient field and the ejecting flux rope. In the present study, the dipole field is assumed as the ambient field and therefore we can integrate the amount of the flux with the following equation:

$$\Phi_D = \int_{\phi_{\min}}^{\phi_{\max}} d\phi \int_{r_{\min}}^{r_{\max}} B_{\theta,D} \left( \theta = \frac{\pi}{2} \right) r dr. \quad (24)$$

Because only the magnetic flux above the spheromak field is relevant to the CME condition, the azimuthal width  $\phi_{\min}, \phi_{\max}$  of the overlying magnetic flux are determined by that of the spheromak field in the initial condition:  $\phi_{\min}, \phi_{\max} = \pm \tan^{-1}(a_S/|\mathbf{r}_S|)$ . Then we obtain the overlying magnetic flux  $\Phi_D = 1.19 \times 10^{-2}$ . On the other hand we can also integrate the poloidal flux of the spheromak field with the equation (20). The azimuthal width in

spheromak coordinate is set to  $\pm\pi/2$  when the upper half of the spheromak field is assumed to commit to their ejection. Then we get  $\Phi_P = 2.45 \times 10^{-3}$ . The relation between amount of magnetic flux  $\Phi_P < \Phi_D$  in case B and C. This condition naturally explains the disappearing of the flux rope due to flux peeling-off reconnection in case B. In case C, the reconnection is not completely anti-parallel and so inefficient that the amount of the stripped magnetic flux is less than that of the flux rope. In case A, there is no obstacle ambient field. Hence, the flux rope in case A and C is not dissipated.

Although only three typical cases are modeled in the present study, there can be any intermediate situations. For example, the ambient field is anti-parallel but total amount of magnetic flux is smaller than that of an ejecting flux rope, the flux rope also retains its shape and escapes to the outer space. Such a condition is a candidate condition where explosive energy release has been studied as the breakout model (Antiochos et al. 1999). In the case of small scale, Galsgaard et al. (2007) and Archontis & Török (2008) studied emerging flux into preexisting and weak coronal field. Galsgaard et al. (2007) showed rising motion of the emerging flux is not affected by the orientation between the emerging flux and the preexisting field. Archontis & Török (2008) showed in anti-parallel case the emerging flux rope successfully erupts while remains confined in other case. In such cases of emerging flux, the amount of emerged magnetic flux becomes more than that of the coronal field within the same spatial scale, because the strength of the magnetic field is very strong in the lower atmosphere. However, since the magnetic field in the real Sun is very complicated, magnetic field in small scale does not necessarily have same direction with global scale field. Furthermore the spatial scale of emerging flux should be (sometimes very) small compared to the solar radius, the flux of global scale ambient field is possibly comparable or larger than that of flux ropes.

In this study, we assume a spheromak field structure smaller than the global scale (the solar radius) and which has a typical amount of magnetic flux  $2.553 \times 10^{21}$  [mx]. The ambient field  $\sim 2.5$  [G] is also comparable to or a little weaker than a typical coronal value. The difference in the direction and the amount of the overlying field leads to much different results. This result may give a hint to understand the observational result that all X-class flares are not necessarily associated with CMEs (Yashiro et al. 2005).

Hence, the overlying field above an eruption region is an important factor for CME formation, and therefore its detail estimation with a realistic corona model is required for CME prediction for space weather forecast. Note that we also did not consider the effect of solar wind which makes substantial amount of magnetic flux open and decreases magnetic obstacle. The detail estimation of amount of magnetic flux using observational data and a realistic corona model is an important task for a CME prediction.

Shiota et al. (2008) discussed a condition for CME formation with 2D simulation of continuously sheared arcade which results in a CME or a confined flux rope formation. They suggested that the condition for CME formation depends on the balance between amounts of the magnetic helicity ( $H$ ) within the flux rope and sheared arcade, and overlying magnetic flux ( $\Phi_{\text{ov}}$ ) which confines the sheared structure, as follows;

$$\frac{\Phi_{\text{ov}}^2}{|H|} < 1.7. \quad (25)$$

In these symmetric condition, maximum energy for the flux rope to escape requires very much due to the work to drag the overlying flux. Therefore the condition of equation (25) is possibly a upper limit for a 3D condition.

The relative magnetic helicity of the each case of the present study, is estimated from the initial condition

$$H = \int (\mathbf{A} + \mathbf{A}_p) \cdot (\mathbf{B} - \mathbf{B}_p) dV, \quad (26)$$

where  $\mathbf{B}_p$  and  $\mathbf{A}_p$  are the potential magnetic field and the corresponding vector potential which are determined by the magnetic field radial component on the inner boundary of the numerical domain. The estimated relative helicity is  $H = -3.65 \times 10^{-4}$ ,  $-2.96 \times 10^{-4}$ ,  $-4.34 \times 10^{-4}$  in case A, B, and C, respectively. The relation of equation (25) for case becomes

$$\frac{\Phi_{\text{ov}}^2}{|H|} = \frac{\Phi_{\text{D}}^2}{|H|} = \frac{(1.19 \times 10^{-2})^2}{4.34 \times 10^{-4}} \sim 0.33 < 1.7. \quad (27)$$

This relation suggests that the confinement due to the overlying field is inefficient to prevent a flux rope escape in case C the results are consistent with the results of Shiota et al. (2008). As same as discussed above, the solar wind decreases the amount of the overlying magnetic flux and help the flux rope to escape from the Sun.

## 4.2. Rotation of ejecting flux rope

As described in §3, the rotations of ejecting flux ropes in the early phase in any cases are caused by the writhe motion of the spheromak structure in the initial conditions. However, the final angles of the escaping flux ropes are quite different ( $\sim 90^\circ$ ) between in case A and C (Figure 2a and 2e). The difference is caused by only the existence of the ambient field, i.e., the interaction between the ejecting flux rope and the ambient field as mentioned in §3.4. The interaction is the reconnection of twisted field within the flux rope to the untwisted ambient field. As a result of reconnection of not completely anti-parallel fluxes, strongly bent magnetic flux can be formed. As the result of a relaxation process of the flux, the flux rope can be rotated.

Angular momentum ( $L_x$ ) and torque( $\tau_x$ ) around the  $x$  axis are obtained from their integral in the space  $V_1 \equiv \{\mathbf{r} | r_{\min} \leq r \leq r_{\max}, \pi/4 \leq \theta \leq 3\pi/4, -\pi/4 \leq \phi \leq \pi/4\}$

$$L_x = \int \int \int_{V_1} dV (\mathbf{r} \times \rho \mathbf{v}) \cdot \hat{\mathbf{x}} \quad (28)$$

$$\tau_x = \int \int \int_{V_1} dV (\mathbf{r} \times \mathbf{F}) \cdot \hat{\mathbf{x}} \quad (29)$$

where  $\mathbf{F}$  expresses any force of Lorentz force, or gradients of gas pressure, or dynamic pressure. The time variations of the torques around the  $x$  axis are shown in Figure 5a and that of angular momentum  $x$  component is shown in Figure 5b. Figures 5a and 5b show that the structure continues to be rotated dominantly by the torque due to the Lorentz force. This result appears that the rotation caused by the writhe motion of the initial flux rope. However, Figure 5c shows the three dimensional distribution of the torque. The net torque mainly works at the surface of the flux rope (indicated pink surfaces emphasized with a white circle in Figure 5c). It appears that the rotation are caused by interaction between magnetic field inside the flux rope and the ambient magnetic field. Magnetic field line which penetrates the strong torque region is drawn with “purple” line in Figure 5c. The “purple” line appears strongly wind, i.e., just after reconnected. This result means that the strong torque regions correspond to the current sheets where the reconnection between the flux rope and the ambient field occurs.

Figure 5d shows a schematic picture of the evolution of the magnetic field lines in case C mentioned above and in §3.4. The expanding flux rope initially rotates counter-clockwise due to its writhe motion. As a result, current sheets are formed at two point on the surface, where the anti-parallel field are contact (indicated with red lines in Figure 5d). Reconnection occurs in the current sheets and then strongly wind field lines (indicated with green and light blue lines in Figure 5d) are formed. The untwisting motion of the winding field causes a strong torque (purple arrows in Figure 5d) which rotates the flux rope.

In a few decades ago, a magnetic field configuration of spheromak in equilibrium state under uniform field has been applied to a laboratory plasma experiment, where plasma must be confined within a device. However, such a spheromak type field configuration is unstable to tilting mode perturbation (Sato & Hayashi 1983). The field configuration settles down where magnetic moment of the spheromak is parallel to the background field. In the nonlinear stage of the instability, the magnetic field causes reconnection which is the same as explained in Figure 5d. The numerical results in this study imply that such an effect in laboratory plasma works also in the coronal plasma.

Such rotations of ejecting flux ropes are reported in some CME observations. Yurchyshyn (2008) investigated the axis angles of magnetic clouds, halo CME axes derived from coro-

nagraph images, and EUV post-eruptive arcade axes in CME source regions. They found that there are good correlation between the axes of EUV arcades and CME angles within a deviation of  $\pm 45^\circ$ . The fact means that some fraction of ejected magnetic structures are significantly rotated during the travels in the lower solar corona but the amount of the rotation is not so much.

The numerical results of the present work are consistent with the observation in that flux ropes can be rotated significantly by the interaction with closed field. However, the rotation angle in case C is more than that of most CMEs in Yurchyshyn (2008). The reason is that the effect of the ambient field in case C is much stronger than the real solar corona because of the following reasons: The dipole field assumed in this study decreases in  $r^{-3}$  with the distance from the Sun  $r$ , and is the potential field whose influence can reach most far away. Most of the dipole field flux are closed because solar wind is not taken into account. Alfvén speed in the simulation is very small because of the assumption of the high plasma density. The slow evolutions allow that the ejecting structure can show enough rotation. The condition in case C is an ideal case to examine the interaction between the ejecting flux rope and the ambient field. Furthermore, although the time evolution in case C is very slow (the terminal CME speed  $\sim 40\text{km s}^{-1}$ ), the terminal speed is comparable to Alfvén speed inside the flux rope.

The rotation process of ejecting flux ropes is also numerically studied by Gibson & Fan (2008) and Lynch et al. (2009). Gibson & Fan (2008) discussed the rotation process with the numerical result of eruption of a twisted flux rope within a potential arcade. They showed that the rotation of the flux rope axis ( $\sim 115^\circ$ ) is caused by the writhe motion. Lynch et al. (2009) discussed the rotation process with the results of two eruptions of arcades sheared oppositely each other. They showed that the opposite chirality of the sheared arcades leads the same amount of opposite rotations of the resulting flux ropes. In contrast to these studies, the results of the present study show that the rotation of the flux rope is affected by not only the writhe motion but the interaction with ambient field as described in §3. Contrast to their works, the results of the present study suggest that an ejecting flux rope can be significantly rotated as a result of reconnection with its ambient field.

### 4.3. Evolution of Anchored Axial flux

In case C, because of the interchange reconnection mentioned in §3.4 the foot points of the ejecting flux rope appear to move outside (colored lines in Figure 3 and 4). In the initial condition only the “green” line was included in the anchored axial flux of the ejecting flux rope, but finally all the “light blue”, “blue” and “red” lines are included. These

changes of anchored foot points are caused by a topological change of magnetic flux due to reconnection in two regions; at the surface and behind of the ejecting flux rope. As described in §3, the ejecting and expanding flux rope forms  $\Omega$ -type loops of the initial axial flux. The first reconnection occurs in the current sheet at the center of the waist of the loop (see the “green” line in Figure 3 and 4). This reconnection severs the anchored axial flux and makes the ejecting flux rope structure detached.

At the same time, the ejecting flux rope reconnects with the ambient field in its side (“light blue” and “blue” lines) and front (the “red” line). In the initial condition of this case, the poloidal field of the flux rope is parallel and therefore unfavorable to reconnection. However the flux rope rotates due to its untwisting (writhe) motion, as described in §4.2. The reconnected ambient field is connected to the inside of the flux rope, i.e., becomes the new axial flux of the ejecting flux rope. The interchange of the anchored axial field makes distance between the legs larger and makes the foot point field strength weaker. As a result, the magnetic tension force can decrease and then the flux rope becomes easier to escape from the Sun.

The interchange of anchored flux explains the evolution of dimming region observed in many flares and/or CMEs with soft X-ray or EUV. In many flares, strong dimming are often observed in both sides of the post eruptive arcades, and there are following weak dimming far from the flare cite (Sterling & Hudson 1997). Such strong dimming can be formed by a sudden expansion of the erupting core and upward dragged overlying flux coupled with coincident rarefaction due to reconnection (Shiota et al. 2005). The following weak dimming are formed by some interaction (stretched or reconnected) with the erupting structure. This evolution of the magnetic field structure is similar to that mentioned by Gibson & Fan (2008). The results of case C in the present study also show that the weak dimming are seen in new footpoints of axial flux formed due to reconnection described in this section.

## 5. Summary

In this study, we performed three global MHD simulations of interaction (magnetic reconnection) between an ejecting flux rope and its ambient field, as a launch process of coronal mass ejections (CMEs). The initial conditions are assumed as ejecting flux ropes under the three different ambient fields: A case without ambient field and cases with dipole field of two opposite directions which are parallel and anti-parallel to that of the flux rope surface. The flux rope can escape to the outer boundary of the numerical domain (evolve to CMEs) in the no ambient case and one dipole case where the direction of ambient field is parallel, while it cannot escape in the other dipole case.

The flux ropes show rotations perpendicular to the ejecting direction, that are caused by not only untwisting (writhe) motion of the flux rope but also the interaction between the ejecting flux rope and the ambient field. Especially, the results show the possibility of rotation due to the relaxation of a complicated field structure which results from the reconnection between the flux rope and the ambient field. The reconnection and resulting rotation are similar to that seen in a spheromak experiment of laboratory plasma.

The results of this study show that the interaction between an ejecting flux rope and its ambient field is a significant process for determining CME formation and CME orientation. For the achievement of space weather forecast it is necessary to predict occurrence of a CME when a flare occurs. A powerful tool for such prediction is MHD simulation of the flare and accompanying ejecting flux rope under a realistic coronal magnetic field.

DS thanks S. Inoue, R. Kataoka, and K. Hayashi for fruitful discussion. The numerical calculation was carried out using the Earth Simulator (ES) in Japan Agency for Marine-Earth Science and Technology (JAMSTEC), under the ES project “Space and Earth System Modeling” (PI: K. Kusano). This work was supported by the Grant-in-Aid for Creative Scientific Research “The Basic Study of Space Weather Prediction” (17GS0208, Head Investigator: K. Shibata) from the Ministry of Education, Culture, Sports, Science, and Technology (MEXT) of Japan and in part by the Grand-in-Aid for the Global COE program “The Next Generation of Physics, Spun from Universality and Emergence” from MEXT of Japan.

## REFERENCES

- Antiochos, S. K., DeVore, C. R., & Klimchuk, J. A. 1999, *ApJ*, 510, 485
- Aoki, S. I., Yashiro, S., & Shibata, K. 2004, *ArXiv Astrophysics e-prints*
- Archontis, V. & Török, T. 2008, *A&A*, 492, L35
- Chen, P. F. & Shibata, K. 2000, *ApJ*, 545, 524
- Choe, G. S. & Lee, L. C. 1996, *ApJ*, 472, 372
- Datlowe, D. W., Elcan, M. J., & Hudson, H. S. 1974, *Sol. Phys.*, 39, 155
- Dedner, A., Kemm, F., Kröner, D., Munz, C.-D., Schnitzer, T., & Wesenberg, M. 2002, *Journal of Computational Physics*, 175, 645
- Dennis, B. R. 1985, *Sol. Phys.*, 100, 465

- Drake, J. F. 1971, *Sol. Phys.*, 16, 152
- Forbes, T. G. & Priest, E. R. 1995, *ApJ*, 446, 377
- Galsgaard, K., Archontis, V., Moreno-Insertis, F., & Hood, A. W. 2007, *ApJ*, 666, 516
- Gibson, S. E. & Fan, Y. 2008, *Journal of Geophysical Research (Space Physics)*, 113, 9103
- Hiei, E., Hundhausen, A. J., & Sime, D. G. 1993, *Geophys. Res. Lett.*, 20, 2785
- Inoue, S. & Kusano, K. 2006, *ApJ*, 645, 742
- Kageyama, A. & Sato, T. 2004, *Geochemistry, Geophysics, Geosystems*, 5, 9005
- Kahler, S. W. 1992, *ARA&A*, 30, 113
- Kataoka, R., Ebisuzaki, T., Kusano, K., Shiota, D., Inoue, S., Yamamoto, T. T., & Tokumaru, M. 2009, *Journal of Geophysical Research (Space Physics)*, 114, 10102
- Kim, Y., Moon, Y., Cho, K., Kim, K., & Park, Y. D. 2005, *ApJ*, 622, 1240
- Kliem, B., Titov, V. S., & Török, T. 2004, *A&A*, 413, L23
- Kliem, B. & Török, T. 2006, *Physical Review Letters*, 96, 255002
- Kusano, K., Maeshiro, T., Yokoyama, T., & Sakurai, T. 2004, *ApJ*, 610, 537
- Lara, A., Gopalswamy, N., Xie, H., Mendoza-Torres, E., Pérez-Erriquez, R., & Michalek, G. 2006, *Journal of Geophysical Research (Space Physics)*, 111, 6107
- Lynch, B. J., Antiochos, S. K., Li, Y., Luhmann, J. G., & DeVore, C. R. 2009, *ApJ*, 697, 1918
- McAllister, A. H., Dryer, M., McIntosh, P., Singer, H., & Weiss, L. 1996, *J. Geophys. Res.*, 101, 13497
- Miyoshi, T. & Kusano, K. 2005, *Journal of Computational Physics*, 208, 315
- Sakajiri, T., Brooks, D. H., Yamamoto, T., Shiota, D., Isobe, H., Akiyama, S., Ueno, S., Kitai, R., & Shibata, K. 2004, *ApJ*, 616, 578
- Sato, T. & Hayashi, T. 1983, *Physical Review Letters*, 50, 38
- Shibata, K. 1999, *Ap&SS*, 264, 129
- Shimizu, T. 1995, *PASJ*, 47, 251

- Shiota, D., Isobe, H., Chen, P. F., Yamamoto, T. T., Sakajiri, T., & Shibata, K. 2005, *ApJ*, 634, 663
- Shiota, D., Kusano, K., Miyoshi, T., Nishikawa, N., & Shibata, K. 2008, *Journal of Geophysical Research (Space Physics)*, 113, 3
- Sterling, A. C. & Hudson, H. S. 1997, *ApJ*, 491, L55+
- Török, T. & Kliem, B. 2005, *ApJ*, 630, L97
- van Leer, B. 1979, *Journal of Computational Physics*, 32, 101
- Yashiro, S., Akiyama, S., Gopalswamy, N., & Howard, R. A. 2006, *ApJ*, 650, L143
- Yashiro, S., Gopalswamy, N., Akiyama, S., Michalek, G., & Howard, R. A. 2005, *Journal of Geophysical Research (Space Physics)*, 110, 12
- Yurchyshyn, V. 2008, *ApJ*, 675, L49
- Yurchyshyn, V., Yashiro, S., Abramenko, V., Wang, H., & Gopalswamy, N. 2005, *ApJ*, 619, 599

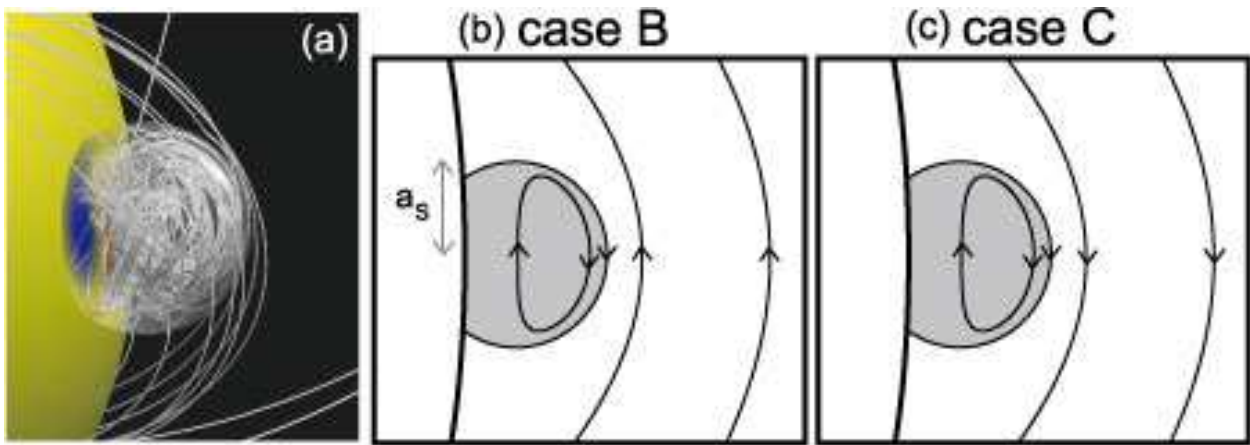


Fig. 1.— (a) Three dimensional view of initial magnetic field in case C. The surface color shows  $B_r$  map and tubes are magnetic field lines. Transparent surface illustrates the surface boundary of the spheromak field. (b) Schematic picture of initial magnetic configuration in the  $y = 0$  plane in case B. Spheromak type field of whose radius is  $a_S$  are assumed in the initial condition (shadowed region). The solid lines express magnetic field lines projected on the  $y = 0$  plane. (c) Schematic picture of initial magnetic configuration in case C shown with the same way as panel (b).

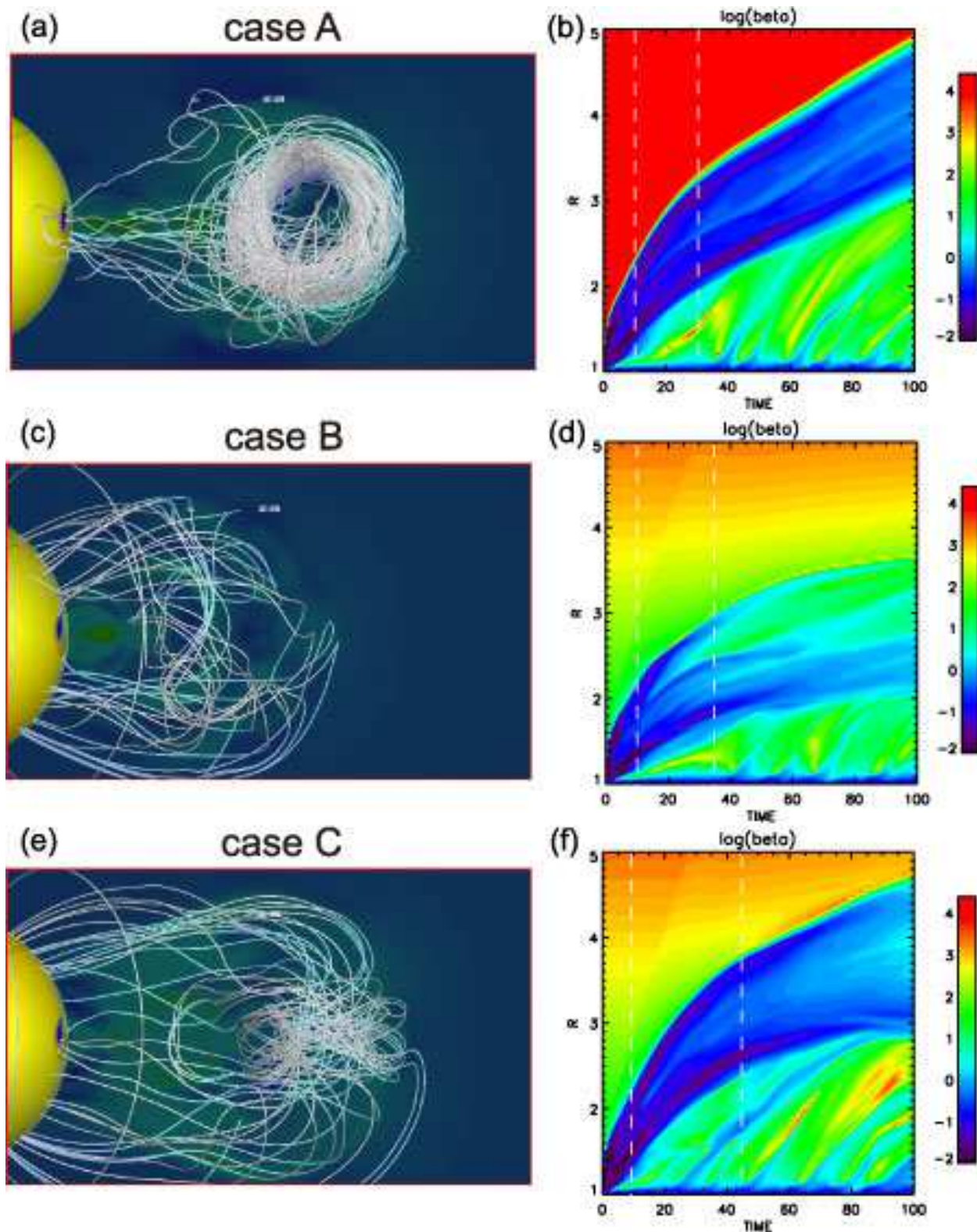


Fig. 2.— (a) Field configurations in late stages ( $t = 50$ ) in case A (no ambient). (b) timeslice of plasma  $\beta$  on the  $x$  axis in case A (no ambient). (c) and (d) are those in case B (anti-parallel), and (e) and (f) are those in case C (parallel), respectively. In the timeslice images, the trajectories of the flux rope are recognized as low  $\beta$  region with rising motion and white dashed lines indicate timing when the evolution of the flux rope changes describes in §3.

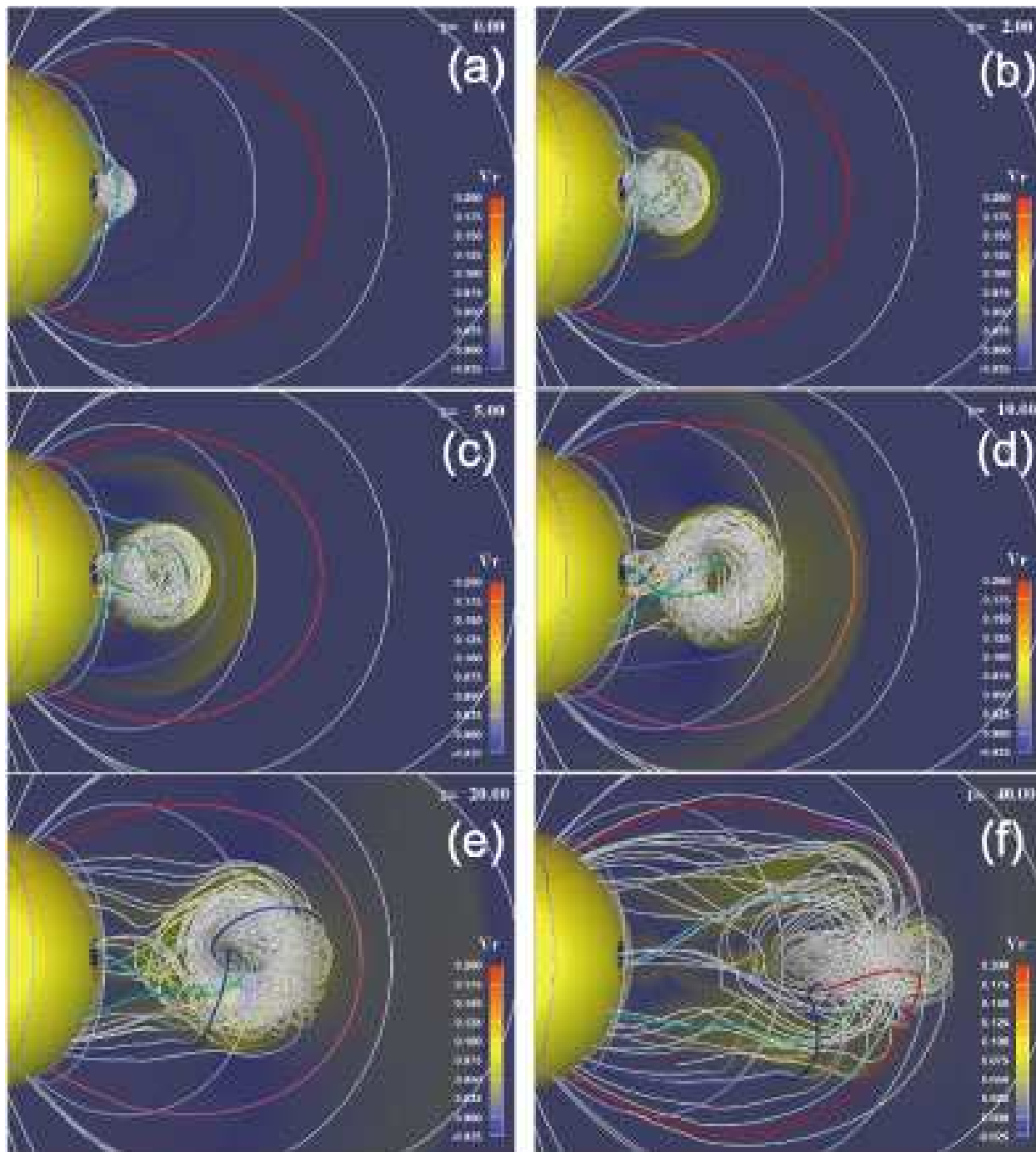


Fig. 3.— Time evolution of magnetic field and velocity in case C. Panels (a) - (f) show those at  $t=0, 2, 5, 10, 20,$  and  $40$ , respectively. The inner boundary is shown with the sphere in the left part of each panel, whose colors indicate  $B_r$  map. The same field lines are displayed with tubes in each panel. Characteristic field lines are colored with green, light blue, blue, and red. The velocity map at  $y = 0$  are displayed with colors on the vertical transparent background.

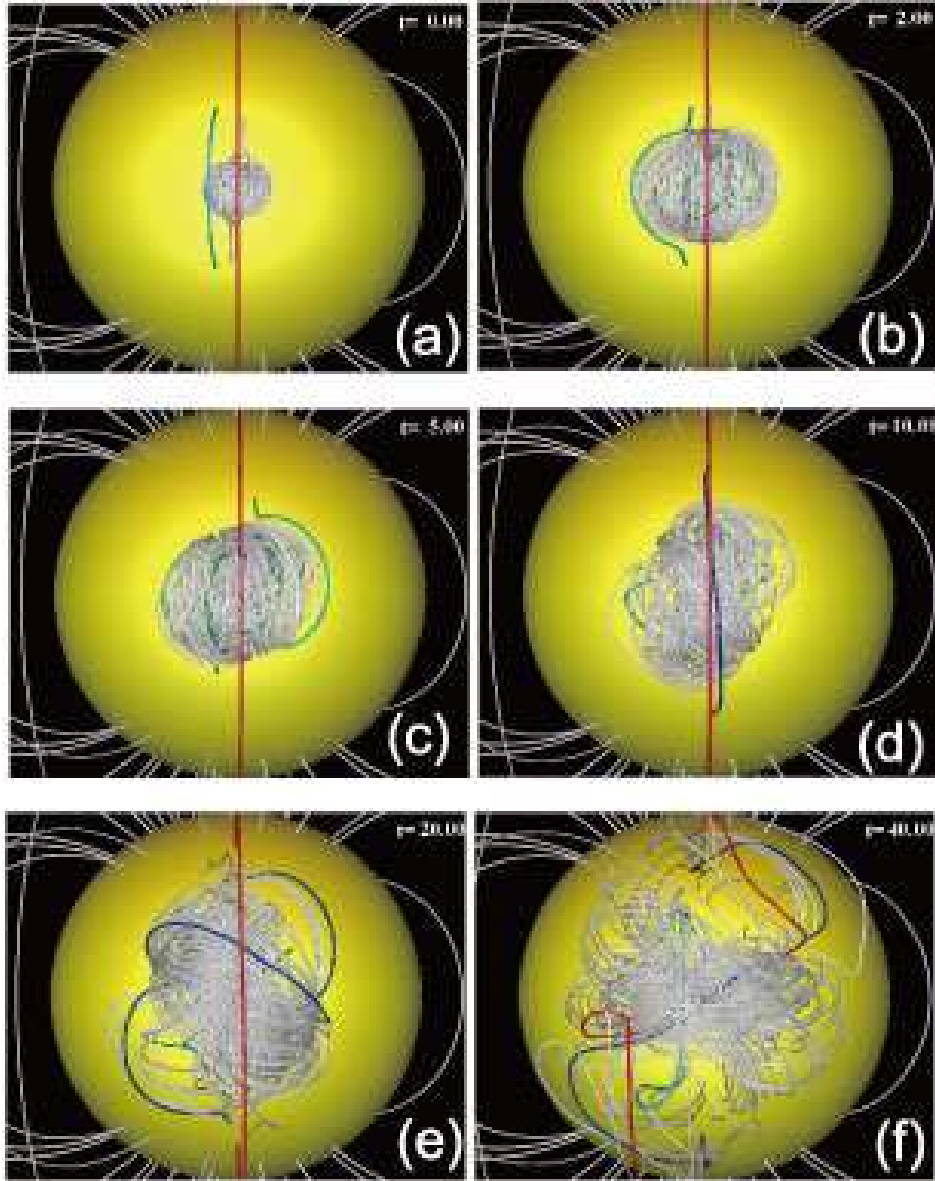


Fig. 4.— Time evolution of face-on view of magnetic field structure in case C. Panels (a) - (f) show those at  $t = 0, 2, 5, 10, 20,$  and  $40,$  respectively. The meaning of the colors on the sphere and the tubes are the same as those in Figure 3

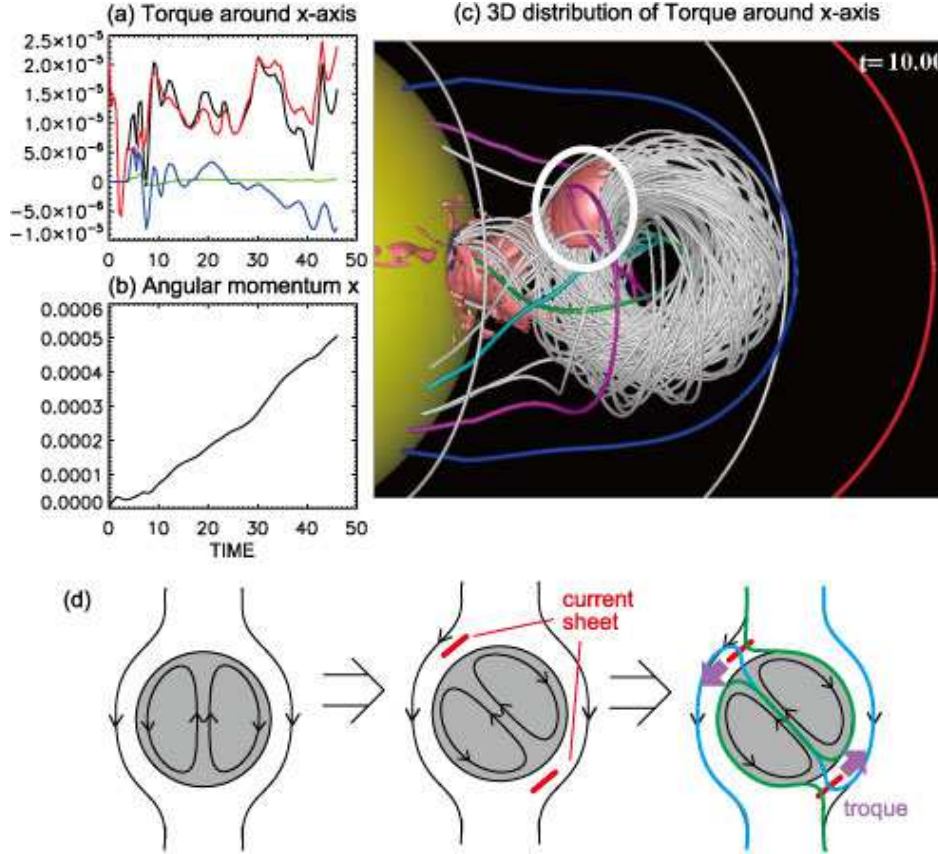


Fig. 5.— Time variation of torques (a) and angular momentum (b) around  $x$ -axis in case C (parallel). Green, blue, red, and black lines in panel (a) show time variations of torques caused by dynamic pressure, gas pressure gradient, Lorentz force, and total force, respectively. (c) Three dimensional distribution of the magnetic torque around the  $x$  axis. Pink surfaces show positions where counter-clockwise (negative  $x$ ) torques work. White circle indicates the position of the net counter-clockwise torque which substantially rotates the flux rope. (d) Schematic pictures of magnetic field lines on a horizontal cross section in the ejecting structure. Due to its writhe motion, the twisted flux rope rotates counter-clockwise (evolution form the left panel to the center panel). As a result, current sheets (indicated with red lines in the center panel) are formed on the partial surface of the flux rope. Reconnection in the sheets produce steep bend magnetic field (green and light blue lines in the right panel of (d) and purple tube in panel (c)), which causes the torque due to the magnetic tension force.